




Submegahertz Nucleation of Plasmonic Vapor Microbubbles near a Solid Vertical Boundary

Fulong Wang (王福龙)¹, Zhibin Hu,¹ Binglin Zeng¹, Chenliang Xia¹, Lihua Dong,¹
Huimin Wang,² Lijun Yang,^{3,4} and Yuliang Wang (王玉亮)^{1,4,*}

¹*Robotics Institute, School of Mechanical Engineering and Automation, Beihang University, Beijing 100191, People's Republic of China*

²*National Center for Materials Service Safety, University of Science and Technology Beijing, Beijing 100083, People's Republic of China*

³*School of Astronautics, Beihang University, Beijing 100191, People's Republic of China*

⁴*Ningbo Institute of Technology, Beihang University, Ningbo 315832, People's Republic of China*



(Received 7 March 2023; accepted 27 June 2024; published 5 August 2024)

Laser triggered and photothermally induced vapor bubbles have emerged as promising approaches to facilitate optomechanical energy conversion for numerous applications in microfluidics and nanofluidics. Here, we report an observation of spontaneously triggered periodic nucleation of plasmonic vapor bubbles near a rigid sidewall with readily tuned nucleation frequency from 0.8 kHz to over 200 kHz. The detailed collapsing process of the vapor bubbles was experimentally and numerically investigated. We find that the lateral migration of residual bubbles toward the sidewall refreshes the laser spot area, terminates the subsequent steady bubble growth, and leads to the repeatable bubble nucleation. A mathematic model regarding the Kelvin impulses was derived. It shows that the competition between the rigid boundary induced Bjerknes force and laser irradiation caused thermal Marangoni force on collapsing bubbles governs the process. The model also leads to a criterion of $\gamma\zeta < 0.34$ for repeatable bubble nucleation, where γ is the normalized distance and ζ thermal Marangoni coefficient. This study demonstrates nucleation of violent vapor bubbles at extreme high frequencies, providing an approach to remotely realize strong localized flows in microfluidics and nanofluidics.

DOI: [10.1103/PhysRevLett.133.064001](https://doi.org/10.1103/PhysRevLett.133.064001)

Because of the enhanced plasmonic effect, laser irradiated and water immersed noble metal nanoparticles can rapidly produce a huge amount of heat and trigger the nucleation of so called plasmonic bubbles [1–5]. These bubbles have emerged in numerous innovative applications, including cancer therapy [6,7], micromanipulation [8], nanoscale propulsion [2–4], microfabrication [9], and ultrasensitive detection [10]. The nucleation of plasmonic bubbles involves rich physicochemical hydrodynamics [11,12]. Exploring new phenomena during nucleation and growth of these bubbles helps to expand their applications.

The nucleation of plasmonic microbubbles experiences four sequential life phases [5,13]: an explosively growing and rapidly collapsing giant vapor bubble [phase 1, hereafter referred to as initial plasmonic bubble (IPB)] [13,14], an oscillating bubble (phase 2) [15,16], and two steadily growing phases, phases 3 and 4, dominated by vaporization and gas diffusion, respectively [5]. The ultrashort lifetime (~ 10 μ s) and extremely fast expansion speed of IPBs (~ 20 m/s) indicate the possibility of remotely achieving strong localized flows with modulation frequency up to

hundreds of kilohertz [13,17,18], which will be astonishing in lab-on-a-chip devices. These microfluidics-nanofluidics devices normally operate with low Reynolds number laminar flows, due to the huge area-to-volume ratios [19,20]. As a result, there is a high demand of localized strong flows to efficiently carry out various basic operations, such as mixing, pumping, sorting, and propulsion [21–26]. However, as mentioned earlier, IPBs are inevitably followed by the subsequent three life phases. Exploring the possibility of sustained periodic nucleation of IPBs without subsequent life phases is attractive.

In this study, we report an observation of spontaneously triggered periodic nucleation of IPBs with a frequency f over 200 kHz nearby a rigid boundary. We explore how the competition between the Bjerknes force induced by rigid boundary and the thermal Marangoni force determines the migration direction of collapsing IPBs, which in turn governs periodic bubble nucleation.

Experiments were conducted on water-immersed gold nanoparticle (GNP) decorated substrates. In the experiments, the substrates were irradiated by a continuous wave laser of 532 nm wavelength near a fabricated polydimethylsiloxane (PDMS) vertical sidewall. Images were captured in an optical setup (Fig. S1 in Supplemental

*Contact author: wangyuliang@buaa.edu.cn

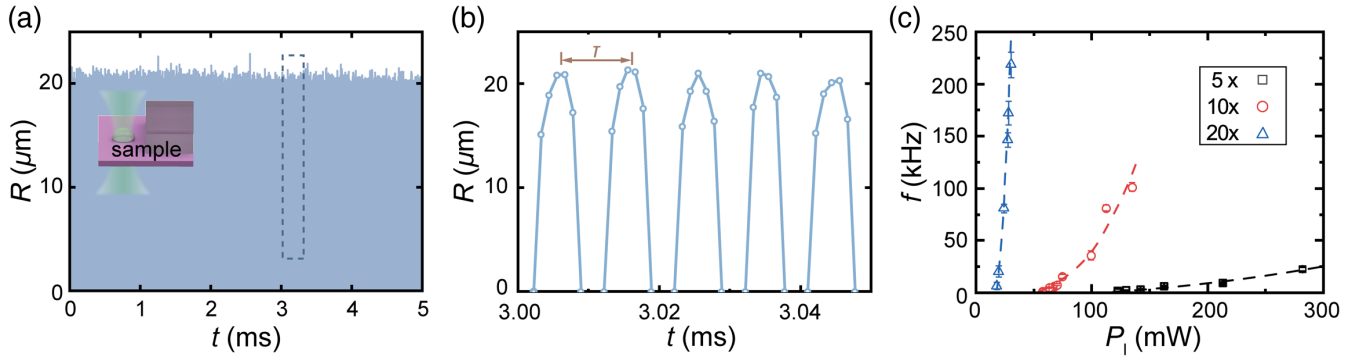


FIG. 1. Periodic nucleation of plasmonic bubbles near a vertical sidewall on a GNP decorated sample surface. (a) Temporal evolution of radius R for 500 repeatedly nucleated IPBs in 5 ms, corresponding to a nucleation frequency f of 100 kHz. The inset diagram illustrates the laser spot area nearby a vertical sidewall. (b) $R-t$ curve for five selected cycles from (a). (c) Nucleation frequency f as a function of P_1 for IPBs obtained with different objective lenses. A maximum value of $f = 218.4$ kHz was achieved at $m = 20\times$ and $P_1 = 30.4$ mW.

Material [27]) at a frame rate of 900 kfps. The radius R of the nucleated plasmonic bubbles as a function of time t in 5 ms is depicted in Fig. 1(a), as well as Fig. 1(b) of the enlarged display for the selected area in Fig. 1(a). Remarkably, we find that IPBs can repeatedly nucleate, grow, and collapse at a frequency $f = 100$ kHz (see Movie S1 as well as Fig. S2 [27] for the method to determine f). This is clearly different from the case without the PDMS vertical sidewall, where an IPB was followed by a steadily growing plasmonic bubble (Movie S2, Movie S3, and Fig. S3) [5,13]. The nucleation frequency f rapidly increases with laser power P_1 [Fig. 1(c)]. As demonstrated in Movie S4, different nucleation frequencies of 5.4, 9, 18, 39, and 80 kHz were obtained for P_1 values of 62.5, 67.6, 74.3, 99.0, and 112.3 mW, respectively, using a 10 \times objective lens. Moreover, by changing the magnification m of the focusing objectives, f can be readily tuned from 0.8 kHz to 218.4 kHz ($m = 20\times$ and $P_1 = 30.4$ mW). This is about 2 orders of magnitude higher than what has been achieved so far [23,24]. Since the lifetime of a micro-sized vapor bubble is a few microseconds [36], this submegahertz frequency is very close to the critical value one can achieve for repeatable nucleation of microbubbles.

Figure 2(a)(i) and Movie S5 show sequentially captured bottom view images of an IPB with a lifetime of 23.3 μ s. Note that the time in Fig. 2(a) is normalized by bubble's lifetime τ_c . The bubble first rapidly grows and reaches its maximum size at around $t/\tau_c = 0.48$ and then quickly collapses. The lateral centroid position L_{bub} and corresponding lateral displacement $\Delta = L_{\text{las}} - L_{\text{bub}}$ of IPBs were obtained. During its entire lifetime, Δ keeps changing (Fig. S4 [27]). Near the end of the collapse period ($t/\tau_c: 0.86 \rightarrow 1$), the bubble quickly moves toward the sidewall. Bubble displacement at the moment of bubble collapse is denoted as Δ_{τ_c} .

The observed migration of IPBs near the sidewall was consistent with that obtained in a boundary integration method (BIM) simulation [33,34], as shown in Fig. 2(a)(ii)

and Movie S6. For details of the BIM simulation, please refer to the section *The BIM simulation of bubble dynamics* in the Supplemental Material. For simplicity, the simulation ignores the supporting substrate and focuses on the impact of the sidewall on the dynamics of IPBs. The left and right parts in each subfigure in Fig. 2(a)(ii) correspond to the constructed pressure and velocity fields, respectively. It clearly shows that the pressure asymmetrically distributes

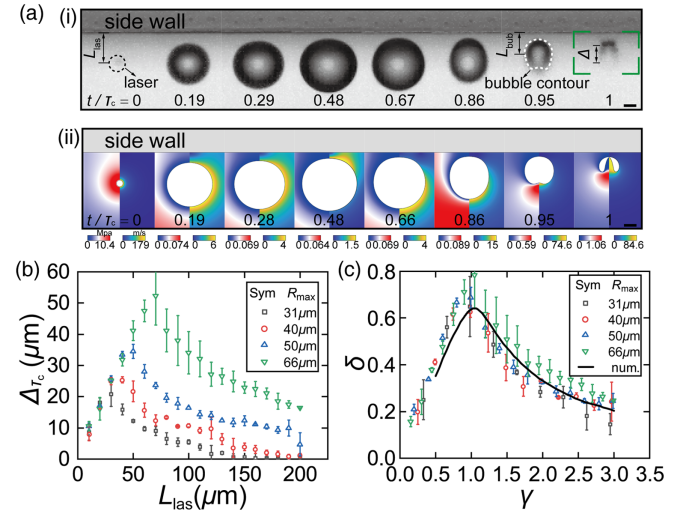


FIG. 2. Characterization of bubble motion near a vertical sidewall. (a)(i) Sequential bottom view optical images of an IPB near a sidewall along its entire life cycle. L_{las} and L_{bub} denote the lateral distance of the centers of the laser spot and the IPB to the sidewall, respectively, while Δ represents the displacement of the collapsing bubble toward the vertical sidewall (scale bar: 40 μ m, $R_{\text{max}} \approx 90$ μ m, and $L_{\text{las}} = 100$ μ m). (a)(ii) Numerically simulated temporal evolution of the pressure field (left) and velocity field (right) around a vapor bubble near a sidewall. (b) Bubble displacement Δ_{τ_c} at $t/\tau_c = 1$ as a function of L_{las} for bubbles with different R_{max} of 31, 40, 50, and 66 μ m. (c) $\delta = \Delta_{\tau_c}/R_{\text{max}}$ as a function of $\gamma = L_{\text{las}}/R_{\text{max}}$ for IPBs with different R_{max} . The black solid line is from the BIM simulation.

around the IPB, resulting in a net liquid pressure and, consequently, the Bjerknes force [37–39] applied on IPBs. As a result, the IPB is significantly displaced from the laser spot during the collapse period. This refreshes the surrounding fluid field and makes it ready for the nucleation of the following repeated IPBs.

To gain further insights in the process, L_{las} was systematically adjusted from 10 to 200 μm with a step size of 10 μm for IPBs with different R_{max} . The bubble displacement Δ_{τ_c} (at $t/\tau_c = 1$) as a function of L_{las} is depicted in Fig. 2(b). Despite changed R_{max} , all bubbles exhibit a similar trend. As L_{las} decreases from 200 μm , Δ_{τ_c} first increases, reaches a maximum value, and then decreases. Δ_{τ_c} and L_{las} were further normalized with respect to R_{max} as $\delta = \Delta_{\tau_c}/R_{\text{max}}$ and $\gamma = L_{\text{las}}/R_{\text{max}}$. Interestingly, we find the normalized curves collapse on each other for bubbles with different R_{max} and δ reaches its maximum value at $\gamma = 1$ [Fig. 2(c)]. It implies that the influence of the Bjerknes force diminishes as γ exceeds 1. Additionally, the decreased δ with decreasing γ in the region of $1 > \gamma > 0$ is due to the impact of water jets and the restriction of the nearby sidewall. The observed $\delta - \gamma$ dependence was further validated numerically using the BIM [black solid curve in Fig. 2(c)].

It is now evident that the collapsing IPBs can be displaced nearby the sidewall. Figure 3(a) and Movie S7 depict how the sidewall changes the motion of three typical IPBs of $R_{\text{max}} \approx 42 \mu\text{m}$ as well as their residual bubbles after IPB collapse. For an IPB with $L_{\text{las}} = 60 \mu\text{m}$, it moves toward the sidewall during the collapse period. After that, its residual bubble rapidly moves toward the sidewall. As a result, no bubble remains on the laser spot area. For an IPB with $L_{\text{las}} = 110 \mu\text{m}$, the influence of the sidewall diminishes. The residual bubble moves back to the laser spot area, leaving a tiny bubble nucleus there. The third IPB nucleated on a GNP decorated substrate without the sidewall ($L_{\text{las}} = \infty$). It collapses and leaves a bubble nucleus in the laser spot area. In the latter two

scenarios, the remaining tiny bubble nuclei initiate the subsequent two steadily growing phases. As a result, repeatable bubble nucleation cannot take place. Therefore, the lateral distance L_{las} is a key parameter in governing the periodic nucleation of IPBs. L_{las} should be sufficiently small to ensure a strong Bjerknes force and hence a large enough lateral displacement Δ_{τ_c} to guarantee the periodic IPB nucleation.

Next, we further investigated the required lateral displacement Δ_{τ_c} to trigger the periodic IPB nucleation. To do so, probability maps of the periodic nucleation for IPBs with different R_{max} were constructed using 10 \times and 5 \times objective lenses. An example of such maps is shown in Fig. 3(b). It describes the ratio of periodic nucleation durations to a specific value (50 ms in this case) at each L_{las} position in ten experiments. It is obvious that periodic nucleation can successfully take place when $L_{\text{las}} < 90 \mu\text{m}$ but ceases when L_{las} exceeds 120 μm . The duration of periodic nucleation rapidly decreases within the range of $90 \mu\text{m} < L_{\text{las}} < 120 \mu\text{m}$, which is taken as the transition region (TR). We extracted Δ_{τ_c} for ten IPBs in the center of the TR [$L_{\text{las}} = 100 \mu\text{m}$ in Fig. 3(b)] and calculated their average value $\Delta_{\tau_c, \text{TR}}$ as 15.5 μm . In the TR, γ varies from 1.5 to 2.5. According to the curve shown in Fig. 2(c), δ or Δ_{τ_c} monotonically decreases with γ in this range. Therefore, $\Delta_{\tau_c, \text{TR}}$ can be taken as the minimum Δ_{τ_c} value to guarantee periodic IPB nucleation. This in turn determines a maximum γ value for periodic bubble nucleation. The value $\Delta_{\tau_c, \text{TR}}$ extracted from individual probability maps is shown in Fig. 3(c). Interestingly, it clearly shows that $\Delta_{\tau_c, \text{TR}}$ remains almost constant at 16.7 and 34.0 μm for the 10 \times and 5 \times objective lenses, respectively, regardless of different R_{max} . The reason for the constant $\Delta_{\tau_c, \text{TR}}$ will be explained later.

One may wonder why the bubble with $L_{\text{las}} = 110 \mu\text{m}$ in Fig. 3(a) first moves a considerable distance toward the sidewall, then turns around, and eventually returns to the laser spot area. Upon laser irradiation, the GNP decorated sample surface rapidly produces a significant amount of heat, resulting in a locally elevated temperature

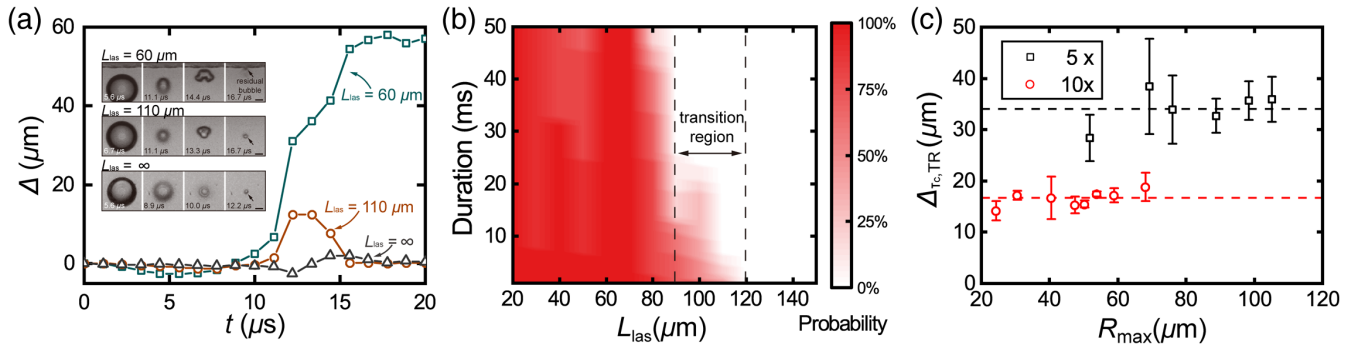


FIG. 3. Correlation between residual bubble position and periodic bubble nucleation. (a) Bubble displacement Δ as a function of t for three IPBs with different L_{las} . The inset shows the sequential optical images of the collapsing bubbles. (b) Probability map showing periodic nucleation of IPBs by changing L_{las} from 20 to 150 μm ($R_{\text{max}} = 50 \mu\text{m}$). (c) Average value of Δ_{τ_c} in the transition region (TR) for bubbles with different R_{max} .

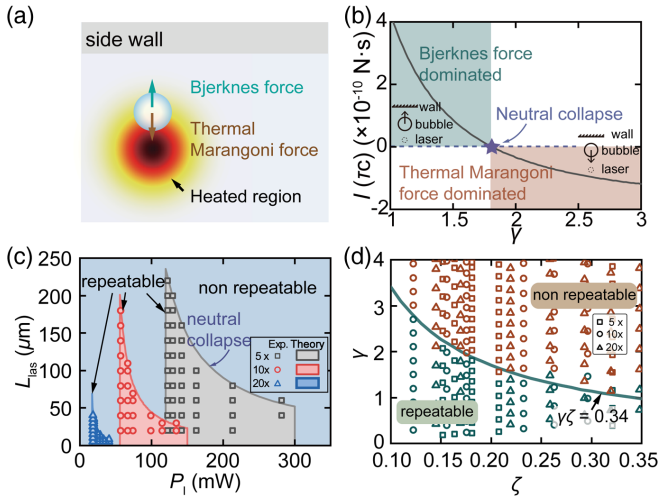


FIG. 4. Determination of regimes of repeatable bubble nucleation. (a) A schematic diagram depicting the competition between the sidewall induced Bjerknes force and thermal Marangoni force applied on bubble around the laser spot area. (b) An exemplary curve of Kelvin impulse $I(\tau_c)$ versus γ at $R_{\max} = 40 \mu\text{m}$ and $P_1 = 74 \text{ mW}$. (c) Determined regimes of periodic bubble nucleation in a $L_{\text{las}}-P_1$ two-dimensional parameter space. The symbols represent experimental data and the solid curves are theoretically determined boundaries of the periodic nucleation regimes. (d) Normalized experimental data in a $\gamma-\zeta$ parameter space. The solid curve is the theoretically predicted boundary of repeatable and nonrepeatable regimes based on $\gamma\zeta = 0.34$.

field [11,40,41]. This creates a strong temperature gradient and, consequently, a surface tension gradient along the radial direction of the laser spot. As a result, thermal Marangoni force applies to bubbles, competing with the Bjerknes force, and pulling the off-centered bubble back to the laser spot area, as illustrated in Fig. 4(a). Thus, the motion dynamics of the residual bubbles after IPB collapse depends on the relative strength of these two forces.

To reveal this competition mechanism, the Kelvin impulse $I(t) = \int_0^t F(t)dt$ applied on IPBs was estimated. Here, $F(t)$ is the external net force. The Kelvin impulse can be regarded as the momentum of a vapor bubble and is used to determine its motion [33,37,42,43]. For simplicity, the dynamics of IPBs is approximated as a time-varying point source or sink, represented by the volume growth rate $q(t) = 4\pi R^2 dR/dt = \pm 4\pi R^2 \{2(p_\infty - p_v)/3\rho [(R_{\max}/R)^3 - 1]\}^{1/2}$ of IPBs, where ρ is water density, p_v and p_∞ are saturated vapor pressure and atmosphere pressure, respectively. In the equation, the bubble surface velocity dR/dt was derived from the Rayleigh equation $(p_v - p_\infty)/\rho = R d^2R/dt^2 + 3/2(dR/dt)^2$ [36]. The positive and negative sign correspond to the growth or collapse phases of IPBs. For detailed derivation of $q(t)$, please refer to Supplemental Material [27].

Since the contribution of bubble migration to the velocity potential is negligible, the source or sink is assumed to be at

a fixed position of L_{las} relative to the sidewall [38]. Besides, the temperature gradient ∇T is assumed to be constant and is proportional to laser power [11,35]. The pinning force between IPBs and the substrate is estimated to be approximately $0.1 \mu\text{N}$ and is negligible compared to Bjerknes and thermal Marangoni force (see Supplemental Material for details [27]). Therefore, $F(t)$ mostly includes Bjerknes force and the thermal Marangoni force, and can thus be given as $F = \rho q(t)/16\pi L_{\text{las}}^2 - 2\pi R^2 \nabla T d\sigma/dT$, where σ is the surface tension coefficient [37,44]. By substituting $q(t)$ and $F(t)$ into $I(t)$, one can obtain the expression of the Kelvin impulse as

$$I(t) = \frac{\pi R_{\max}^5}{9L_{\text{las}}^2} \sqrt{6\Delta p \rho} C_1(t) - \pi R_{\max}^3 \sqrt{\frac{2\rho}{3\Delta p}} \frac{d\sigma}{dT} \nabla T C_2(t), \quad (1)$$

where $\Delta p = p_\infty - p_v$, $C_1(t) = B_\alpha(7/6, 3/2)$, and $C_2(t) = B_\alpha(3/2, 1/2)$ for $0 \leq t \leq \tau_c/2$, $C_1(t) = 2B(7/6, 3/2) - B_\alpha(7/6, 3/2)$ and $C_2(t) = 2B(3/2, 1/2) - B_\alpha(3/2, 1/2)$ for $\tau_c/2 \leq t \leq \tau_c$. Here, $B(a, b)$ and $B_\alpha(a, b)$ are complete and incomplete beta functions, respectively, and $\alpha = (R(t)/R_{\max})^3$.

The resulting Kelvin impulse $I(\tau_c)$ yields the directional motion of vapor bubbles [37]. Here, an exemplary $I(\tau_c) - \gamma$ curve is depicted in Fig. 4(b). For a lower value of γ , the Kelvin impulse is positive, resulting in a Bjerknes force dominated migration. As a result, residual bubbles migrate toward the sidewall, enabling the periodic nucleation. In contrast, for a larger γ , the Kelvin impulse is negative. The motion of the residual bubble is dominated by thermal Marangoni force and hence moves back to the laser spot area. The periodic bubble nucleation is then terminated. At a specific value of γ , the Kelvin impulse is zero, as indicated by a purple star in Fig. 4(a). This condition is called neutral collapse where IPBs do not exhibit obvious directional migration [45]. It can also be treated as the boundary of periodic nucleation regimes.

To validate the above theory, the regimes of the repeatable bubble nucleation in the $P_1 - L_{\text{las}}$ parameter space were experimentally established, as shown in Fig. 4(c). In the figure, the markers represent successfully triggered periodic nucleation of IPBs in experiments for different objective lenses of 5 \times , 10 \times , and 20 \times . The solid curves are the theoretically determined boundaries of nonrepeatable and repeatable regimes, corresponding to the neutral collapse of IPBs. One can see that the experimentally determined regimes of repeatable IPB nucleation match well with the theoretically defined ones. For details of theoretical calculations of the boundary curves, please refer to ‘‘Theoretical boundaries of periodic bubble nucleation regimes’’ in Supplemental Material [27]. For each objective lens, IPB size decreases with increasing P_1 (Fig. S5), leading to a reduced available range of L_{las} .

By taking $I(\tau_c) = 0$ in Eq. (1), the boundary between the regimes of repeatable and nonrepeatable bubble collapse defined by the neutral collapse of IPBs can be theoretically determined. Remarkably, this leads us to a simple expression as

$$\gamma\zeta = \sqrt{\frac{1 B(7/6, 3/2)}{3 B(3/2, 1/2)}} \approx 0.34, \quad (2)$$

where $\zeta = (\nabla T / \Delta p d \sigma / dT)^{1/2}$ indicates the strength of the thermal Marangoni force and hence is defined as the thermal Marangoni coefficient. Equation (2) can be used to predict whether the repeatable IPB nucleation takes place or not. In the case of $\gamma\zeta < 0.34$, the residual bubbles migrate toward the sidewall, leading to the periodic nucleation. In contrast, the residual bubbles move back to the laser spot area when $\gamma\zeta > 0.34$. The criterion defined by Eq. (2) was further verified experimentally. In Fig. 4(d), the green data points and brown data points correspond to the repeatable and nonrepeatable IPB nucleation, respectively. One can see that for IPBs produced by different objective lenses of 5 \times , 10 \times , and 20 \times , the data points can be well segmented by the boundary defined by $\gamma\zeta = 0.34$. By using the criterion defined by Eq. (2), the relationship between the critical lateral displacement of IPBs ($\Delta_{rc,TR}$) and R_{max} can be theoretically determined (Fig. S6), which is consistent with that shown in Fig. 3(d).

In conclusion, we report the observation of spontaneously triggered periodic nucleation of plasmonic vapor bubbles with a tunable frequency from 0.8 to over 200 kHz. The presence of a nearby rigid boundary results in the symmetry breaking and hence the lateral motion of residual bubbles during bubble collapse. This refreshes the laser spot area, leading to the repeatable nucleation of the vapor bubbles. A theoretical model of Kelvin impulse was derived to unveil the underlying mechanism of competition between the Bjerknes force and the thermal Marangoni force. This further leads to a simple criterion of $\gamma\zeta < 0.34$ for repeatable bubble nucleation, which is in a good agreement with the experimental results. This work reveals the dynamics of vapor bubbles near a sidewall in an uneven temperature field and presents an efficient approach to implement optomechanical energy conversion in microfluidics or nanofluidics.

Acknowledgments—We appreciate Professor Chao Sun from Tsinghua University for fruitful discussion and Buyun Chen from Beihang University for improvement of the image processing algorithm. This work was supported by Natural Science Foundation of China (Grant No. 52075029), Beijing Natural Science Foundation (Grant No. 3232009) and “the Fundamental Research Funds for the Central Universities”.

- [1] G. Baffou, R. Quidant, and C. Girard, *Phys. Rev. B* **82**, 165424 (2010).
- [2] X. Fu, B. Chen, J. Tang, and A. H. Zewail, *Sci. Adv.* **3**, e1701160 (2017).
- [3] E. Lee, D. Huang, and T. Luo, *Nat. Commun.* **11**, 2404 (2020).
- [4] E. Lee and T. Luo, *Sci. Adv.* **6**, eaz3646 (2020).
- [5] Y. Wang, M. E. Zaytsev, H. L. The, J. C. T. Eijkel, H. J. W. Zandvliet, X. Zhang, and D. Lohse, *ACS Nano* **11**, 2045 (2017).
- [6] J. Jeon, D. G. You, W. Um, J. Lee, C. H. Kim, S. Shin, S. Kwon, and J. H. Park, *Sci. Adv.* **6**, eaaz8400 (2020).
- [7] E. Y. Lukianova-Hleb, X. Y. Ren, R. R. Sawant, X. W. Wu, V. P. Torchilin, and D. O. Lapotko, *Nat. Med.* **20**, 778 (2014).
- [8] S. Tokonami, S. Kurita, R. Yoshikawa, K. Sakurai, T. Suehiro, Y. Yamamoto, M. Tamura, O. Karthaus, and T. Iida, *Sci. Adv.* **6**, eaaz5757 (2020).
- [9] J. Li, E. H. Hill, L. Lin, and Y. Zheng, *ACS Nano* **13**, 3783 (2019).
- [10] Y. Liu, H. Ye, H. Huynh, C. Xie, P. Kang, J. S. Kahn, and Z. Qin, *Nat. Commun.* **13**, 1687 (2022).
- [11] B. Zeng, K. L. Chong, Y. Wang, C. Diddens, X. Li, M. Detert, H. J. W. Zandvliet, and D. Lohse, *Proc. Natl. Acad. Sci. U.S.A.* **118**, e2103215118 (2021).
- [12] M. Hu, F. Wang, L. Chen, P. Huo, Y. Q. Li, X. Gu, K. L. Chong, and D. S. Deng, *Nat. Commun.* **13**, 5749 (2022).
- [13] Y. Wang *et al.*, *Proc. Natl. Acad. Sci. U.S.A.* **115**, 7676 (2018).
- [14] Y. Zhang and A. Prosperetti, *Int. J. Heat Mass Transfer* **167**, 120814 (2021).
- [15] F. Li, S. R. Gonzalez-Avila, D. M. Nguyen, and C.-D. Ohl, *Phys. Rev. Fluids* **2**, 014007 (2017).
- [16] K. Namura, S. Okai, S. Kumar, K. Nakajima, and M. Suzuki, *Adv. Mater. Interfaces* **7**, 2000483 (2020).
- [17] X. Li *et al.*, *J. Phys. Chem. C* **123**, 23586 (2019).
- [18] M. E. Zaytsev, G. Lajoinie, Y. L. Wang, D. Lohse, H. J. W. Zandvliet, and X. H. Zhang, *J. Phys. Chem. C* **122**, 28375 (2018).
- [19] D. Huh, B. D. Matthews, A. Mammoto, M. Montoya-Zavala, H. Y. Hsin, and D. E. Ingber, *Science* **328**, 1662 (2010).
- [20] M. Yafia *et al.*, *Nature (London)* **605**, 464 (2022).
- [21] V. Blickle and C. Bechinger, *Nat. Phys.* **8**, 143 (2012).
- [22] S. Krishnamurthy, S. Ghosh, D. Chatterji, R. Ganapathy, and A. K. Sood, *Nat. Phys.* **12**, 1134 (2016).
- [23] S. Jones, D. Andren, T. J. Antosiewicz, and M. Kall, *Nano Lett.* **19**, 8294 (2019).
- [24] S. Jones, D. Andren, T. J. Antosiewicz, A. Stilgoe, H. Rubinsztein-Dunlop, and M. Kall, *ACS Nano* **14**, 17468 (2020).
- [25] P. A. Quinto-Su, *Nat. Commun.* **5**, 5889 (2014).
- [26] F. Schmidt, A. Magazzu, A. Callegari, L. Biancofiore, F. Cichos, and G. Volpe, *Phys. Rev. Lett.* **120**, 068004 (2018).
- [27] See Supplemental Material at <http://link.aps.org/supplemental/10.1103/PhysRevLett.133.064001>, which includes Refs. [28–35], for additional information about the experimental methods, details of the numerical simulations and theoretical model, and supplemental movies.

- [28] D. Obreschkow, M. Bruderer, and M. Farhat, *Phys. Rev. E* **85**, 066303 (2012).
- [29] B. Taib, G. Doherty, and J.R. Blake, *Proc. Centre Math. Appl.* **6**, 166 (1984), <https://projecteuclid.org/ebooks/proceedings-of-the-centre-for-mathematics-and-its-applications/Mathematical-Programming-and-Numerical-Analysis-Workshop/chapter/Boundary-integral-methods-applied-to-cavitation-bubble-dynamics/pcma/1416337607?tab=ArticleFirstPage>.
- [30] R. Tadmor, *Langmuir* **37**, 6357 (2021).
- [31] X. Li *et al.*, *Nat. Phys.* **18**, 713 (2022).
- [32] B. Zeng, Y. Wang, M. E. Zaytsev, C. Xia, H. J. W. Zandvliet, and D. Lohse, *Phys. Rev. E* **102**, 063109 (2020).
- [33] J. R. Blake and D. C. Gibson, *Annu. Rev. Fluid Mech.* **19**, 99 (1987).
- [34] O. Supponen, D. Obreschkow, M. Tinguely, P. Kobel, N. Dorsaz, and M. Farhat, *J. Fluid Mech.* **802**, 263 (2016).
- [35] X. Li, F. Wang, C. Xia, H. L. The, J. G. Bomer, and Y. Wang, *Small* **19**, 2302939 (2023).
- [36] L. Rayleigh, *London Edinburgh Dublin Phil. Mag. J. Sci.* **34**, 94 (1917).
- [37] J. R. Blake, B. B. Taib, and G. Doherty, *J. Fluid Mech.* **170**, 479 (1986).
- [38] J. P. Best and J. R. Blake, *J. Fluid Mech.* **261**, 75 (1994).
- [39] J. R. Blake, D. M. Leppinen, and Q. Wang, *Interface Focus* **5**, 20150017 (2015).
- [40] G. Baffou, P. Berto, E. B. Urena, R. Quidant, S. Monneret, J. Polleux, and H. Rigneault, *ACS Nano* **7**, 6478 (2013).
- [41] S. Jones, D. Andren, P. Karpinski, and M. Kall, *ACS Photonics* **5**, 2878 (2018).
- [42] J. R. Blake, *ANZIAM J.* **30**, 127 (1988).
- [43] D. Obreschkow, M. Tinguely, N. Dorsaz, P. Kobel, A. de Bosset, and M. Farhat, *Phys. Rev. Lett.* **107**, 204501 (2011).
- [44] C. E. Brennen, *Cavitation and Bubble Dynamics* (Cambridge University Press, Cambridge, England, 2013).
- [45] S.-M. Li, A. M. Zhang, P. Cui, S. Li, and Y.-L. Liu, *J. Fluid Mech.* **962**, A28 (2023).